Quantum transport of a spin-1 chiral fermion

Risako Kikuchi,[1] Takumi Funato,[2,3] and Ai Yamakage[1]
[1]*Department of Physics, Nagoya University, Nagoya 464-8602, Japan*
[2]*Center for Spintronics Research Network, Keio University, Yokohama 223-8522, Japan*
[3]*Kavli Institute for Theoretical Sciences, University of Chinese Academy of Sciences, Beijing 100190, China*

(Received 6 June 2022; revised 5 October 2022; accepted 9 November 2022; published 13 December 2022)

We theoretically study the quantum transport in a three-dimensional spin-1 chiral fermion system in the presence of impurity scattering. Within the self-consistent Born approximation, we find peak structure of the density of states and significant suppression of electrical conductivity around the zero energy. The zero-energy conductivity depends less on impurity concentration, unlike a Weyl fermion. These properties originate from the flat-band structure of the spin-1 chiral fermion.

DOI: 10.1103/PhysRevB.106.235204

I. INTRODUCTION

A variety of chiral quasiparticles beyond Weyl and Dirac fermions can emerge in crystalline material, protected by symmetry and topological charges [1]. The spin-1 chiral fermion is a prominent realization of such an exotic particle, which hosts the trivial band with nearly flat dispersion, called the flat band, in addition to the Dirac cone. Angle-resolved photoemission spectroscopy (ARPES) measurements observed a spin-1 chiral fermion in a chiral crystal CoSi [2–6]. A two-dimensional (approximate) version of the spin-1 chiral fermion has also been predicted [7] in the context of the $\alpha-T_3$ lattices. Quantum phenomena, including spin transport [8] and optical responses [9–16], can be anomalous, stemming from the peculiar electronic states of a spin-1 fermion. Research has also spilled over into quadratic dispersion with the spin-1 structure [17–19]. A fundamental example of such phenomena is the electrical conductivity of quantum transport.

Chiral fermions of Dirac and Weyl fermions exhibit peculiar transport properties on zero energy [20–22]. For two-dimensional massless Dirac fermions, representing low-energy electrons in graphene, the electrical conductivity remains finite and independent of the relaxation time at their gapless point, though the density of states vanishes [23–29]. Weyl fermions in the three spatial dimensions, on the other hand, show a specific quantum transport phenomenon strongly depending on the impurity concentration at the Weyl point located on the zero energy [30–34]. Interestingly, a finite(long)-range disorder potential (does not) gives rise to the semimetal–metal transition. These studies imply that the quantum transport phenomena on the zero energy possibly depend on the spatial dimension, disorder type, and symmetry/topology of chiral fermions. Therefore, a spin-1 chiral fermion, characterized by the flat band, monopole charge 2, and orthogonal symmetry class, is expected to show a distinct quantum transport character. Recent years have seen remarkable progress in our understanding of two-dimensional spin-1 systems [35–38]. Thus, we can address quantum transport phenomena in three-dimensional spin-1 systems.

In this work, we theoretically analyze the quantum transport of three-dimensional spin-1 chiral fermion under impurity potentials, based on the Boltzmann transport theory and the self-consistent Born approximation (SCBA) in linear response theory. As a result, we find some characteristic phenomena near the zero energy by SCBA intrinsic to the spin-1 nature. There is a peak structure of the density of states, which originates from a flat band of the spin-1 fermion, depending on the impurity concentration. We also find significant suppression of conductivity near the zero energy. This phenomenon of low-energy transport is caused by the vanishing group velocity of the flat band and the interband effect between the flat band and the Dirac cone.

The paper is organized as follows. Our model for a spin-1 chiral fermion in the presence of impurity is introduced in Sec. II. The conductivity is calculated within the Boltzmann theory in Sec. III and the SCBA with the current vertex correction in Sec. IV. The self-consistent equation for self energy and the Bethe-Salpeter equation for vertex correction are explicitly derived. The comparisons of our results to related works and some remarks are discussed in Sec. V. Section VI summarizes this work.

II. MODEL

We consider a three-dimensional spin-1 chiral fermion system, described by

$$\hat{\mathcal{H}} = \hbar v \hat{\boldsymbol{S}} \cdot \boldsymbol{k}, \tag{1}$$

where $\boldsymbol{k}$ is the electron wave number and v is the Fermi velocity. $\boldsymbol{S} = (\hat{S}_x, \hat{S}_y, \hat{S}_z)$ are the spin operators

$$\hat{S}_x = \begin{pmatrix} 0 & i & 0 \\ -i & 0 & 0 \\ 0 & 0 & 0 \end{pmatrix}, \tag{2}$$

$$\hat{S}_y = \begin{pmatrix} 0 & 0 & -i \\ 0 & 0 & 0 \\ i & 0 & 0 \end{pmatrix}, \tag{3}$$

$$\hat{S}_z = \begin{pmatrix} 0 & 0 & 0 \\ 0 & 0 & i \\ 0 & -i & 0 \end{pmatrix}. \tag{4}$$

The eigenenergy is given by

$$\epsilon_{\lambda,\boldsymbol{k}} = \hbar v \lambda k, \tag{5}$$

where λ is the label for the conduction band ($\lambda = 1$), the flat band ($\lambda = 0$), and the valence band ($\lambda = -1$).

We assume two impurity potentials, the Gaussian and delta function potentials, which represent finite-range and short-range disorders, respectively. Note that the lengthscale of impurity may strongly affect the transport property of chiral fermion systems, as seen in graphene. The Gaussian potential is defined by

$$U(\boldsymbol{r}) = \frac{\pm u_0}{(\sqrt{\pi} d_0)^3} \exp\left(-\frac{r^2}{d_0^2}\right), \tag{6}$$

where d_0 is the characteristic lengthscale and $\pm u_0$ is the strength of the impurity potential. The sign $\pm$ means to assume that the numbers of positive- and negative-valued impurities are the same, so the Fermi level is fixed, irrelevant to the impurity concentration. The delta function potential is defined by

$$U(\boldsymbol{r}) = \pm u_0 \delta(\boldsymbol{r}), \tag{7}$$

which corresponds to the short-range limit ($d_0 \to 0$) of the Gaussian potential. Their Fourier transforms are obtained to be

$$u(\boldsymbol{k}) = \pm u_0 \exp\left(-\frac{k^2}{q_0^2}\right), \tag{8}$$

with $q_0 = 2/d_0$ and $u(\boldsymbol{k}) = \pm u_0$, respectively. To avoid the ultraviolet divergence, we need to regularize the delta function potential with a hard cutoff as

$$u(\boldsymbol{k}) = \pm u_0 \theta(q_0 - k), \tag{9}$$

where q_0 is the inverse of the length that characterizes the impurity potential. Both Eqs. (8) and (9) tend to be of the delta function for $q_0 \to \infty$. The position representation of Eq. (9) can be written in the form

$$\int \frac{d^3k}{(2\pi^3)} e^{i\boldsymbol{k}\cdot\boldsymbol{r}} u(\boldsymbol{k}) = \frac{-q_0 r \cos(q_0 r) + \sin(q_0 r)}{r^3}. \tag{10}$$

At $q_0 \to \infty$, the first term is a fast oscillating function and the integral can be regarded as zero. The second term corresponds to the zero-order spherical Bessel function $J_0(q_0 r)$.

Isotropic disorder potentials are characterized by the moment of scattering angle as

$$V_n^2(k, k') = 2\pi \int_{-1}^{1} d(\cos\theta_{\boldsymbol{k}\boldsymbol{k}'}) |u(\boldsymbol{k} - \boldsymbol{k}')|^2 \cos^n \theta_{\boldsymbol{k}\boldsymbol{k}'}, \tag{11}$$

where $\theta_{\boldsymbol{k}\boldsymbol{k}'}$ is the angle between $\boldsymbol{k}$ and $\boldsymbol{k}'$. We also define a parameter characterizing the scattering strength

$$W = \frac{q_0 n_{\rm i} u_0^2}{\hbar^2 v^2}, \tag{12}$$

where $n_{\rm i}$ is the number of scatterers per unit volume.

III. BOLTZMANN TRANSPORT THEORY

We calculate the conductivity from the Boltzmann transport theory. The scattering probability $W_{\lambda'\boldsymbol{k}',\lambda\boldsymbol{k}}$ is given by Fermi's golden rule as

$$W_{\lambda'\boldsymbol{k}',\lambda\boldsymbol{k}} = \frac{2\pi}{\hbar} n_{\rm i} |\langle \lambda', \boldsymbol{k}'|U|\lambda, \boldsymbol{k}\rangle|^2 \delta(\epsilon_{\lambda',\boldsymbol{k}'} - \epsilon_{\lambda,\boldsymbol{k}}). \tag{13}$$

The transport relaxation time $\tau_{\rm tr}$ is defined by

$$\frac{1}{\tau_{\rm tr}(\epsilon_{\lambda,\boldsymbol{k}})} = \sum_{\lambda'} \int \frac{d\boldsymbol{k}'}{(2\pi)^3} (1 - \cos\theta_{\boldsymbol{k}'\boldsymbol{k}}) W_{\lambda'\boldsymbol{k}',\lambda\boldsymbol{k}}. \tag{14}$$

The density of states of the linear dispersion ($\lambda = \pm 1$) in the clean limit is given by

$$D_0(\epsilon) = \frac{\epsilon^2}{2\pi^2(\hbar v)^3} \quad \text{for} \quad \epsilon \neq 0, \tag{15}$$

and that of the flat band is ($\lambda = 0$) described by the delta function and diverges for $\epsilon = 0$. The conductivity at the zero temperature is obtained to be

$$\sigma_B(\epsilon) = \frac{e^2 v^2}{3} D_0(\epsilon) \tau_{\rm tr}(\epsilon). \tag{16}$$

The transport relaxation time is written as

$$\begin{aligned} \frac{1}{\tau_{\rm tr}(\epsilon)} &= \frac{n_{\rm i}}{2\pi\hbar^2 v} \int_{-1}^{1} \int_{0}^{\infty} dk' d(\cos\theta_{\boldsymbol{k}\boldsymbol{k}'}) k'^2 (1 - \cos\theta_{\boldsymbol{k}\boldsymbol{k}'}) \\ &\quad \times \frac{(\cos\theta_{\boldsymbol{k}\boldsymbol{k}'} + 1)^2}{4} \delta(k - k') |u(\boldsymbol{k} - \boldsymbol{k}')|^2 \\ &= \frac{n_{\rm i}\epsilon^2}{4(2\pi)^2\hbar(\hbar v)^3} \big[V_0^2(\epsilon/\hbar v, \epsilon/\hbar v) + V_1^2(\epsilon/\hbar v, \epsilon/\hbar v) \\ &\quad - V_2^2(\epsilon/\hbar v, \epsilon/\hbar v) - V_3^2(\epsilon/\hbar v, \epsilon/\hbar v)\big], \end{aligned} \tag{17}$$

where the momentum is located on the Fermi surface, $k = \epsilon/\hbar v$. As a result, we find the conductivity

$$\sigma_B(\epsilon) = \frac{e^2 v^2 \hbar}{\pi n_{\rm i} u_0^2}, \tag{18}$$

for the delta function potential with $q_0 \to \infty$. In addition,

$$\sigma_B(\epsilon) = \frac{8}{3\pi} \frac{e^2}{\hbar} \frac{1}{n_{\rm i} u_0^2} h\left(\frac{\epsilon}{\hbar v q_0}\right), \tag{19}$$

for the Gaussian potential, where we define

$$h(x) = \frac{64x^8}{32x^4 - 16x^2 + 3 - (8x^2 + 3)\exp(-8x^2)}. \tag{20}$$

Figure 1 shows the conductivity for the Gaussian potential, which is a monotonically increasing function of the Fermi energy and takes a finite value at zero energy

$$\sigma_B(\epsilon \to 0) = \frac{e^2 v^2 \hbar}{\pi n_{\rm i} u_0^2}, \tag{21}$$

which coincides with that of the delta function potential. The Fermi-energy dependence of conductivity stems from the wave-number dependence of the potential. The delta- and Gaussian-function potentials are constant and exponentially decreasing functions of the wave number. Therefore the conductivity is constant and an increasing function for the delta and Gaussian potentials, respectively.

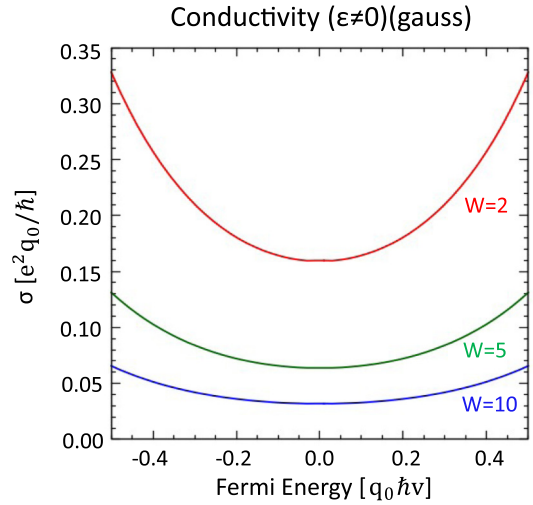

FIG. 1. Electrical conductivity of a spin-1 fermion for $W = 2$ (red line), $W = 5$ (green line), and $W = 10$ (blue line), derived by the Boltzmann equation with the Gaussian potential.

IV. LINEAR RESPONSE THEORY (SCBA)

Next, we calculate the density of states and conductivity in a self-consistent manner to consider the effect of level broadening induced by impurity.

A. Formulation

Assuming that the impurity distribution is uniformly random, the impurity-averaged Green's function is given by

$$\hat{G}(\boldsymbol{k}, \epsilon + is0) = \frac{1}{\epsilon \hat{S}_0 - \hbar v k \hat{\boldsymbol{S}} \cdot \boldsymbol{n} - \hat{\Sigma}(\boldsymbol{k}, \epsilon + is0)}, \tag{22}$$

where $\boldsymbol{n} = \boldsymbol{k}/k$ is the unit vector and $\hat{S}_0$ is the identity matrix. The sign s refers to the retarded ($s = 1$) and advanced ($s = -1$) Green's functions. The self-consistent equation for the self-energy is written as

$$\hat{\Sigma}(\boldsymbol{k}, \epsilon + is0) = \int \frac{d\boldsymbol{k}'}{(2\pi)^3} n_{\rm i} |u(\boldsymbol{k} - \boldsymbol{k}')|^2 \hat{G}(\boldsymbol{k}', \epsilon + is0). \tag{23}$$

The density of states per unit volume is calculated as

$$D(\epsilon) = -\frac{1}{\pi} \mathrm{Im} \int \frac{d\boldsymbol{k}}{(2\pi)^3} \mathrm{Tr} \hat{G}(\boldsymbol{k}, \epsilon + i0). \tag{24}$$

The conductivity by the Kubo formula is written as

$$\sigma(\epsilon) = -\frac{\hbar e^2 v^2}{4\pi} \sum_{s,s'=\pm 1} ss' \int \frac{d\boldsymbol{k}'}{(2\pi)^3} \mathrm{Tr}[\hat{S}_x \hat{G}(\boldsymbol{k}', \epsilon + is0) \times \hat{J}_x(\boldsymbol{k}', \epsilon + is0, \epsilon + is'0) \hat{G}(\boldsymbol{k}', \epsilon + is'0)], \tag{25}$$

where $\hat{J}_x(\boldsymbol{k}, \epsilon, \epsilon')$ is the current density flowing in the x direction reinforced with the vertex correction and is determined to be a solution of the following Bethe-Salpeter equation:

$$\hat{J}_x(\boldsymbol{k}, \epsilon, \epsilon') = \hat{S}_x + \int \frac{d\boldsymbol{k}'}{(2\pi)^3} n_{\rm i} |u(\boldsymbol{k} - \boldsymbol{k}')|^2 \hat{G}(\boldsymbol{k}', \epsilon) \times \hat{J}_x(\boldsymbol{k}', \epsilon, \epsilon') \hat{G}(\boldsymbol{k}', \epsilon'). \tag{26}$$

Since $(\hat{\boldsymbol{S}} \cdot \boldsymbol{n})^3 = (\hat{\boldsymbol{S}} \cdot \boldsymbol{n})$ for the spin-1 representation matrices, the self energy is expressed as

$$\hat{\Sigma}(\boldsymbol{k}, \epsilon) = \Sigma_1(k, \epsilon) \hat{S}_0 + \Sigma_2(k, \epsilon)(\hat{\boldsymbol{S}} \cdot \boldsymbol{n}) + \Sigma_3(k, \epsilon)(\hat{\boldsymbol{S}} \cdot \boldsymbol{n})^2. \tag{27}$$

Using the above expansion, Eq. (22) is rewritten as

$$\hat{G}(\boldsymbol{k}, \epsilon) = \frac{1}{X(k, \epsilon) \hat{S}_0 + Y(k, \epsilon) \hat{\boldsymbol{S}} \cdot \boldsymbol{n} + Z(k, \epsilon)(\hat{\boldsymbol{S}} \cdot \boldsymbol{n})^2} = x(k, \epsilon) \hat{S}_0 + y(k, \epsilon)(\hat{\boldsymbol{S}} \cdot \boldsymbol{n}) + z(k, \epsilon)(\hat{\boldsymbol{S}} \cdot \boldsymbol{n})^2, \tag{28}$$

where

$$X(k, \epsilon) = \epsilon - \Sigma_1(k, \epsilon), \tag{29}$$

$$Y(k, \epsilon) = -\hbar v k - \Sigma_2(k, \epsilon), \tag{30}$$

$$Z(k, \epsilon) = -\Sigma_3(k, \epsilon), \tag{31}$$

and

$$x(k, \epsilon) = \frac{1}{X(k, \epsilon)}, \tag{32}$$

$$y(k, \epsilon) = -\frac{Y(k, \epsilon)}{[X(k, \epsilon) + Z(k, \epsilon)]^2 - Y(k, \epsilon)^2}, \tag{33}$$

$$z(k, \epsilon) = \frac{Y(k, \epsilon)^2 - Z(k, \epsilon)[X(k, \epsilon) + Z(k, \epsilon)]}{\{[X(k, \epsilon) + Z(k, \epsilon)]^2 - Y(k, \epsilon)^2\} X(k, \epsilon)}. \tag{34}$$

Here we reduce the above expressions for the self energy to a form more convenient to solve the self-consistent equation. Substituting Eq. (28) into Eq. (23), we get

$$\begin{aligned} \hat{\Sigma}(\boldsymbol{k}, \epsilon + is0) &= \hat{S}_0 \int \frac{k'^2 dk'}{(2\pi)^3} n_{\rm i} \{V_0^2(k, k') x(k', \epsilon + is0) \\ &\quad + [V_0^2(k, k') - V_2^2(k, k')] z(k', \epsilon + is0)\} \\ &\quad + (\hat{\boldsymbol{S}} \cdot \boldsymbol{n}) \int \frac{k'^2 dk'}{(2\pi)^3} n_{\rm i} V_1^2(k, k') y(k', \epsilon + is0) \\ &\quad + (\hat{\boldsymbol{S}} \cdot \boldsymbol{n})^2 \int \frac{k'^2 dk'}{(2\pi)^3} n_{\rm i}^2 \left(\frac{3}{2} V_2^2(k, k') - \frac{1}{2} V_0^2(k, k') \right) \\ &\quad \times z(k', \epsilon + is0), \end{aligned} \tag{35}$$

with the help of useful relations shown in Appendix A. Comparing this with Eq. (27), the self-consistent equation is decomposed into the three equations as

$$\begin{aligned} \Sigma_1(k, \epsilon + is0) &= \int \frac{k'^2 dk'}{(2\pi)^3} n_{\rm i} \big[V_0^2(k, k') x(k', \epsilon + is0) \\ &\quad + (V_0^2(k, k') - V_2^2(k, k')) z(k', \epsilon + is0) \big], \end{aligned} \tag{36}$$

$$\Sigma_2(k, \epsilon + is0) = \int \frac{k'^2 dk'}{(2\pi)^3} n_{\rm i} V_1^2(k, k') y(k', \epsilon + is0), \tag{37}$$

$$\Sigma_3(k, \epsilon + is0) = \int \frac{k'^2 dk'}{(2\pi)^3} n_{\rm i} \left(\frac{3}{2} V_2^2(k, k') - \frac{1}{2} V_0^2(k, k') \right) \times z(k', \epsilon + is0). \tag{38}$$

Substituting the self energy into Eq. (24), the density of states is written as

$$D(\epsilon) = -\frac{1}{\pi}\mathrm{Im}\int\frac{d\boldsymbol{k}}{(2\pi)^3}\Bigg(\frac{1}{X(k,\epsilon+i0)} + \frac{1}{X(k,\epsilon+i0)+Y(k,\epsilon+i0)+Z(k,\epsilon+i0)} + \frac{1}{X(k,\epsilon+i0)-Y(k,\epsilon+i0)+Z(k,\epsilon+i0)}\Bigg). \tag{39}$$

In addition, the Bethe-Salpeter equation is simplified into an easier form. The current vertex $\hat{J}_x(\boldsymbol{k},\epsilon,\epsilon')$ is expanded to eight terms as

$$\begin{aligned}\hat{J}_x(\boldsymbol{k},\epsilon,\epsilon') = {}& \hat{S}_x J_0(k,\epsilon,\epsilon') + n_x(\hat{\boldsymbol{S}}\cdot\boldsymbol{n})^2 J_1(k,\epsilon,\epsilon') \\ & + n_x(\hat{\boldsymbol{S}}\cdot\boldsymbol{n})J_2(k,\epsilon,\epsilon') + (\hat{\boldsymbol{S}}\cdot\boldsymbol{n})^2\hat{S}_x J_3(k,\epsilon,\epsilon') \\ & + \hat{S}_x(\hat{\boldsymbol{S}}\cdot\boldsymbol{n})^2 J_4(k,\epsilon,\epsilon') + (\hat{\boldsymbol{S}}\cdot\boldsymbol{n})\hat{S}_x J_5(k,\epsilon,\epsilon') \\ & + \hat{S}_x(\hat{\boldsymbol{S}}\cdot\boldsymbol{n})J_6(k,\epsilon,\epsilon') + n_x\hat{S}_0 J_7(k,\epsilon,\epsilon'),\end{aligned} \tag{40}$$

by using Eqs. (A7) to (A11) for Eq. (26) (see Appendix A). The matrix-form Bethe-Salpeter equation reduces to the eight equations (see Appendix B) for the expansion coefficients J_0−J_7. Substituting them into Eq. (25), the conductivity is written as

$$\begin{aligned}\sigma(\epsilon) = {}& \frac{2\hbar e^2 v^2}{3}\int_0^\infty \frac{k'^2 dk'}{(2\pi)^3}\mathrm{Re}\Bigg[-\frac{J_0^{++}+J_1^{++}+J_2^{++}+J_3^{++}+J_4^{++}+J_5^{++}+J_6^{++}+J_7^{++}}{(X+Y+Z)^2} \\ & - \frac{J_0^{++}-J_1^{++}+J_2^{++}+J_3^{++}+J_4^{++}-J_5^{++}-J_6^{++}-J_7^{++}}{(X-Y+Z)^2} - \frac{2J_0^{++}+J_3^{++}+J_4^{++}+J_5^{++}+J_6^{++}}{X(X+Y+Z)} \\ & - \frac{2J_0^{++}+J_3^{++}+J_4^{++}-J_5^{++}-J_6^{++}}{X(X-Y+Z)} + \frac{J_0^{+-}+J_1^{+-}+J_2^{+-}+J_3^{+-}+J_4^{+-}+J_5^{+-}+J_6^{+-}+J_7^{+-}}{|X+Y+Z|^2} \\ & + \frac{J_0^{+-}-J_1^{+-}+J_2^{+-}+J_3^{+-}+J_4^{+-}-J_5^{+-}-J_6^{+-}-J_7^{+-}}{|X-Y+Z|^2} + \frac{J_0^{+-}+J_4^{+-}+J_6^{+-}}{X(X^*+Y^*+Z^*)} \\ & + \frac{J_0^{+-}+J_4^{+-}-J_6^{+-}}{X(X^*-Y^*+Z^*)} + \frac{J_0^{+-}+J_3^{+-}+J_5^{+-}}{X^*(X+Y+Z)} + \frac{J_0^{+-}+J_3^{+-}-J_5^{+-}}{X^*(X-Y+Z)}\Bigg],\end{aligned} \tag{41}$$

where $J_i^{ss'} = J_i(k',\epsilon+is0,\epsilon+is'0)$, $X = X(k',\epsilon+i0)$, and so on.

B. Numerical calculations

The self-consistent equations derived above cannot be generally solved in an analytic way, but we can obtain the solution by numerical iteration [29]. We discretize the wave number as

$$dk_j = k_c\frac{j}{\sum_{j=1}^{j_{\max}} j}, \quad k_j = \frac{1}{2}dk_j + \sum_{j'=1}^{j-1} dk_{j'}, \tag{42}$$

where $j = 1, 2, \ldots, j_{\max}$ and k_c is the cutoff wave number. Hereafter, we fix $j_{\max} = 500$.

C. Density of states

The density of states and conductivity are obtained by SCBA. We fix $k_c = q_0$ in the following. Note that the results do not explicitly depend on q_0 because the density of states and the conductivity are functions of $\epsilon/(q_0\hbar v)$ and W, and is normalized by $q_0^2/\hbar v$ and $e^2 q_0/\hbar$, respectively.

Figures 2(a-1) and 2(a-2) show the density of states as a function of the Fermi energy for the delta function and Gaussian potentials, respectively. We can see a pronounced peak structure around the zero energy. This peak stems from the flat band at $\epsilon = 0$ and is broadened by the impurity potential. Away from the zero energy, the density of states is approximately proportional to ϵ^2, which comes from the linear dispersion bands and is essentially the same as those in the clean limit.

D. Conductivity

Figures 2(b-1) and 2(b-2) show the conductivity as a function of the Fermi energy for the delta function and Gaussian potentials, respectively. In the high-energy region, for both the delta function/Gaussian potential, the conductivity increases monotonically and reaches nearly the values given in the Boltzmann theory. However, the conductivity is significantly suppressed in the vicinity of the zero energy. The energy range of the suppressed area is as wide as that of the peak of the density of states. This implies that the flat band plays a crucial role in suppressing conductivity.

In addition, the suppressed conductivity exhibits a behavior specific to the lengthscale of the potential. Figures 2(c-1) and 2(c-2) show enlarged views of the suppressed area. The conductivity for the delta function potential [Fig. 2(c-1)] shows a small peak, whereas that for the Gaussian potential [Fig. 2(c-2)] is nearly constant with a tiny dip in the zero energy. This difference is due to the vertex corrections J_1-J_7 in Eq. (40). We clarified that the suppressed conductivity for the Gaussian potential without vertex correction ($J_0 = 1, J_1 = J_2 = \ldots = J_7 = 0$) makes a small peak, the same as for the delta function potential. Namely, the vertex correction plays a vital role in the low-energy regime. Unlike the Gaussian potential, the conductivity for the delta function potential

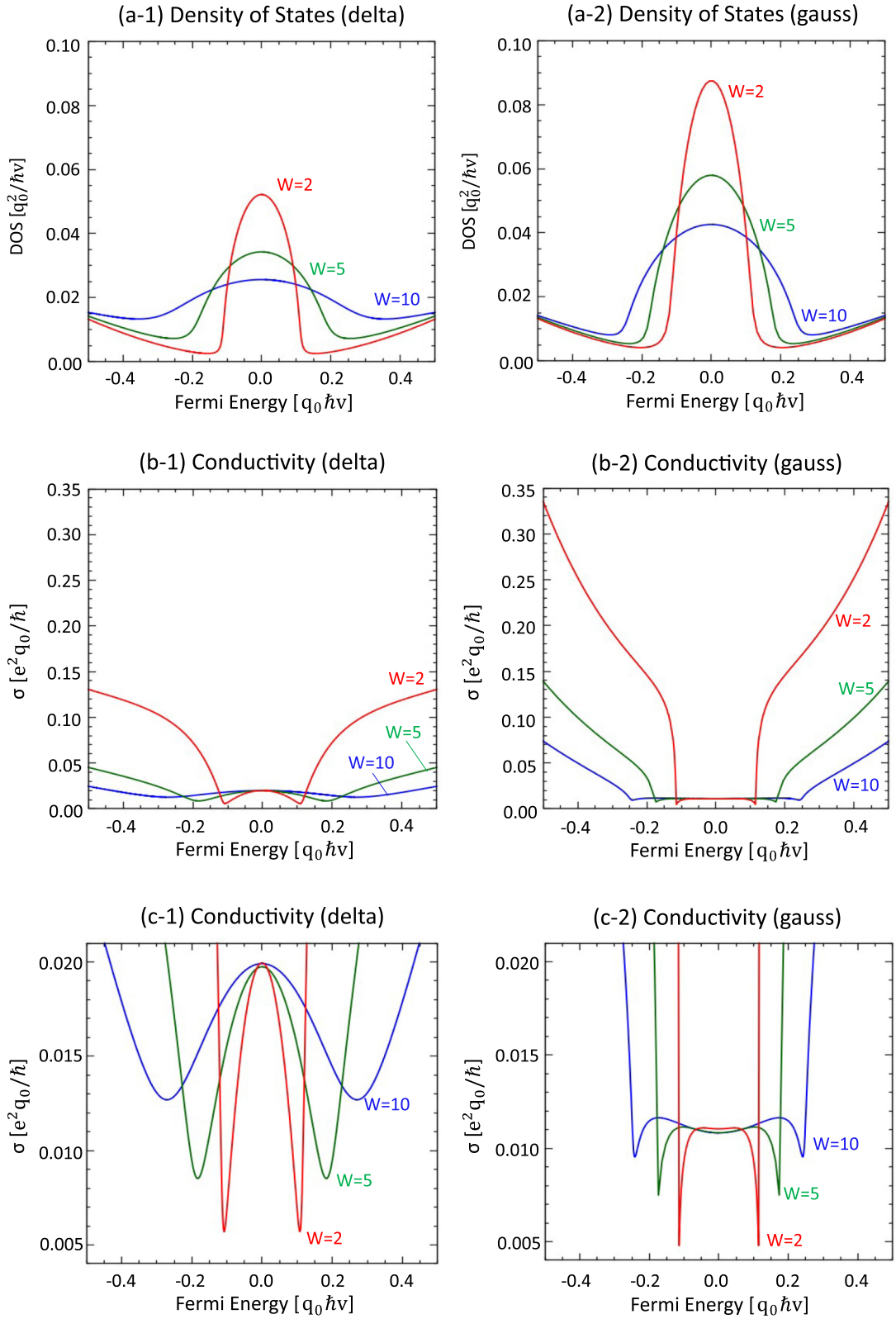

FIG. 2. Quantum transport for $W = 2$ (red line), $W = 5$ (green line), and $W = 10$ (blue line), derived by the SCBA. Density of states for (a-1) the delta function potential and (a-2) Gaussian potential ($k_c = q_0$). Conductivity for (b-1) the delta function potential and (b-2) the Gaussian potential ($k_c = q_0$). (c-1) and (c-2) are the enlargements near the zero energy of (b-1) and (b-2), respectively.

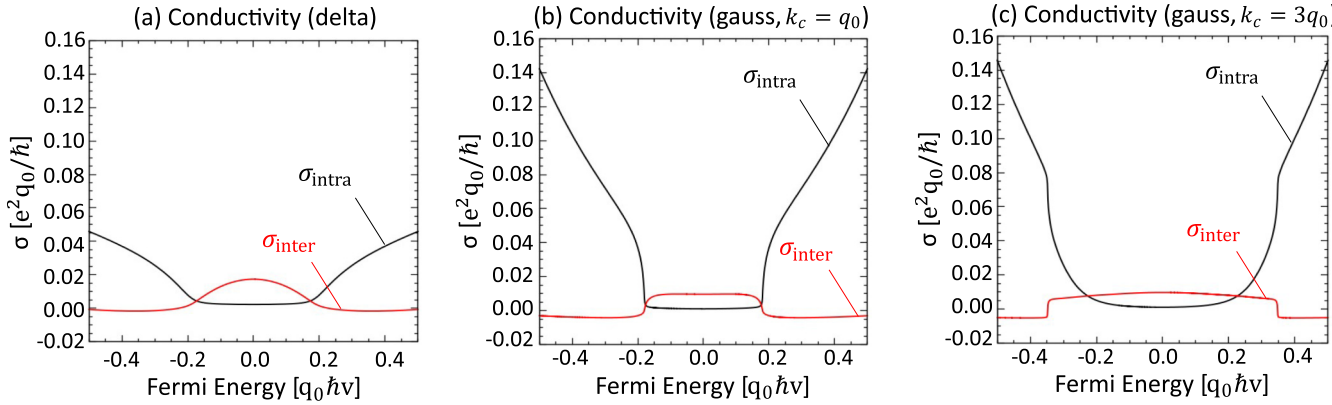

FIG. 3. The conductivity from the intraband transition of the Dirac cone (black line) and from the interband transition between the Dirac cone and the flat band (red line) for $W = 5$ derived by the SCBA. (a) Delta function potential, (b) Gaussian potential $k_c = q_0$, and (c) Gaussian potential $k_c = 3q_0$.

produces a small peak and is not flattened by the vertex correction, which is given by $J_0 \neq 0$ and $J_1 = J_2 = \ldots = J_7 = 0$. Note that the suppressed conductivity shows less dependence on W than the unsuppressed area in the higher energy.

In this study, we assume zero temperature. The conductivity at a finite temperature is given by $\int d\epsilon(-\partial f/\partial\epsilon)\sigma(\epsilon)$. The Fermi-energy dependence of the conductivity is smeared by the Fermi distribution f. In spin-1 systems, since the conductivity has a large Fermi-energy dependence, the temperature dependence may be nonmonotonic.

E. Interband effect

Here we clarify the details of the characteristic behavior near zero energy and its origin. To do so, we decompose the conductivity into intraband and interband contributions, which are defined by

$$\sigma_{\rm intra}(\epsilon) = -\frac{\hbar e^2 v^2}{4\pi}\sum_{s,s'=\pm1} ss' \int \frac{d\boldsymbol{k}'}{(2\pi)^3}\big(S_{cc}G_c^s J_{cc}^{ss'} G_c^{s'} + S_{vv}G_v^s J_{vv}^{ss'} G_v^{s'}\big), \tag{43}$$

and

$$\sigma_{\rm inter}(\epsilon) = -\frac{\hbar e^2 v^2}{4\pi}\sum_{s,s'=\pm1} ss' \int \frac{d\boldsymbol{k}'}{(2\pi)^3}\big(S_{0c}G_c^s J_{c0}^{ss'} G_0^{s'} + S_{c0}G_0^s J_{0c}^{ss'} G_c^{s'} + S_{0v}G_v^s J_{v0}^{ss'} G_0^{s'} + S_{v0}G_0^s J_{0v}^{ss'} G_v^{s'}\big), \tag{44}$$

where the subscripts c, 0, and v denote the conduction, flat, and valence bands in the band basis, respectively. They are obtained by diagonalizing the Green's function matrix as

$$\hat{U}^\dagger \hat{G}(\boldsymbol{k}, \epsilon + is0)\hat{U} = \begin{pmatrix} G_c^s & 0 & 0 \\ 0 & G_0^s & 0 \\ 0 & 0 & G_v^s \end{pmatrix}. \tag{45}$$

In this basis, the velocities S_x and J_x are written as

$$\hat{U}^\dagger \hat{S}_x \hat{U} = \begin{pmatrix} S_{cc} & S_{c0} & 0 \\ S_{0c} & 0 & S_{0v} \\ 0 & S_{v0} & S_{vv} \end{pmatrix}, \tag{46}$$

and

$$\hat{U}^\dagger \hat{J}_x(k, \epsilon + is0, \epsilon + is'0)\hat{U} = \begin{pmatrix} J_{cc}^{ss'} & J_{c0}^{ss'} & 0 \\ J_{0c}^{ss'} & J_{00}^{ss'} & J_{0v}^{ss'} \\ 0 & J_{v0}^{ss'} & J_{vv}^{ss'} \end{pmatrix}. \tag{47}$$

The flat band has zero velocity leading to the absence of intraband terms. The interband terms between the conduction and valence bands are also zero.

Figure 3 shows the decomposed conductivities in the band basis. One can see a small peak of the interband term and suppression of the intraband terms near $\epsilon = 0$. Namely, the interband conductivity is more dominant than the intraband one. This suggests that disorder effects are decisive for the low-energy transport behavior.

F. Cutoff dependence

Figure 4 is the result of varying the value of k_c in Eq. (42) for the Gaussian potential. Note that we fix $W = 5$ here. One can see that the peak of the density of states shown in Fig. 4 rapidly increases as k_c increases. Our model has an entirely flat band, which is a simple approximation for that in the actual material. Namely, the cutoff momentum k_c corresponds to the range over which the band can be approximated as flat. Consequently, as k_c increases, the contribution from the flat band also increases, resulting in a large peak structure in the density of states.

The conductivity shown in Fig. 4(b) indicates that the energy region showing the suppressed conductivity ($\sigma \sim 0.011e^2q_0/\hbar$) becomes wider as k_c increases for the same reason as for the enhancement of the density of states discussed above. We also find that the conductivity at $\epsilon \sim 0$ does not change significantly with k_c [Fig. 4(c)]. As the density of states increases, the number of scattering channels also increases, and as a result, the conductivity is expected to remain nearly constant.

V. DISCUSSION

A. Comparison of results from Boltzmann equation and SCBA

Figure 5 compares the conductivity derived from the Boltzmann equation with that derived from SCBA. The specific

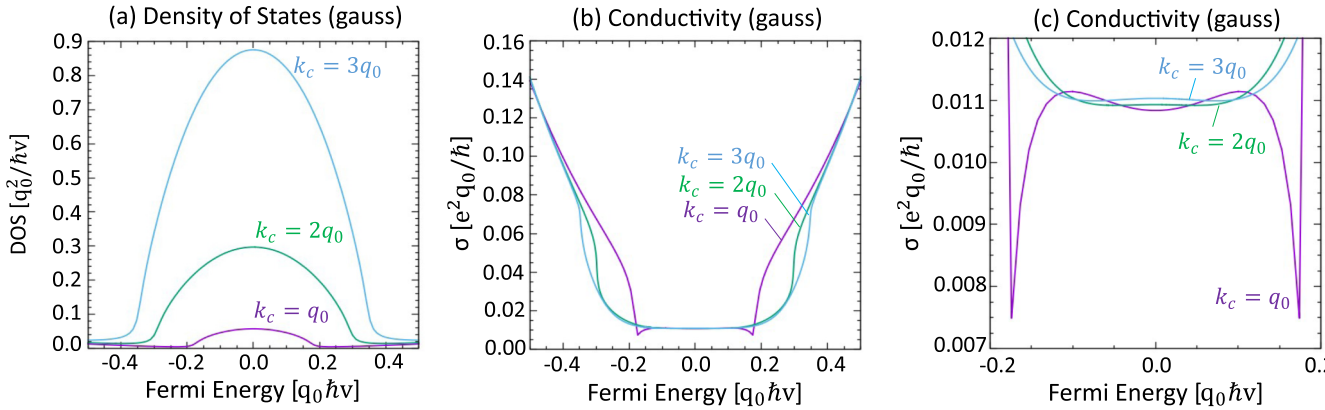

FIG. 4. Quantum transport for $k_c = q_0$ (purple line), $k_c = 2q_0$ (green line), and $k_c = 3q_0$ (blue line) derived by the SCBA. (Gaussian potential, $W = 5$). (a) Density of states, (b) conductivity, and (c) conductivity near the suppressed area.

behavior of the low-energy region (suppressed conductivity) derived from SCBA cannot be derived from the Boltzmann equation for the following reasons. The suppressed conductivity originates from the interband effects of the Dirac cone and the flat band broadened by impurity scattering. The spectral broadening is not considered in the Boltzmann equation hence the interband effect does not contribute to the conductivity, owing to the energy conservation. SCBA is the simplest method to take spectral broadening into account and it provides a simple way to understand interband conduction phenomena in spin-1 systems.

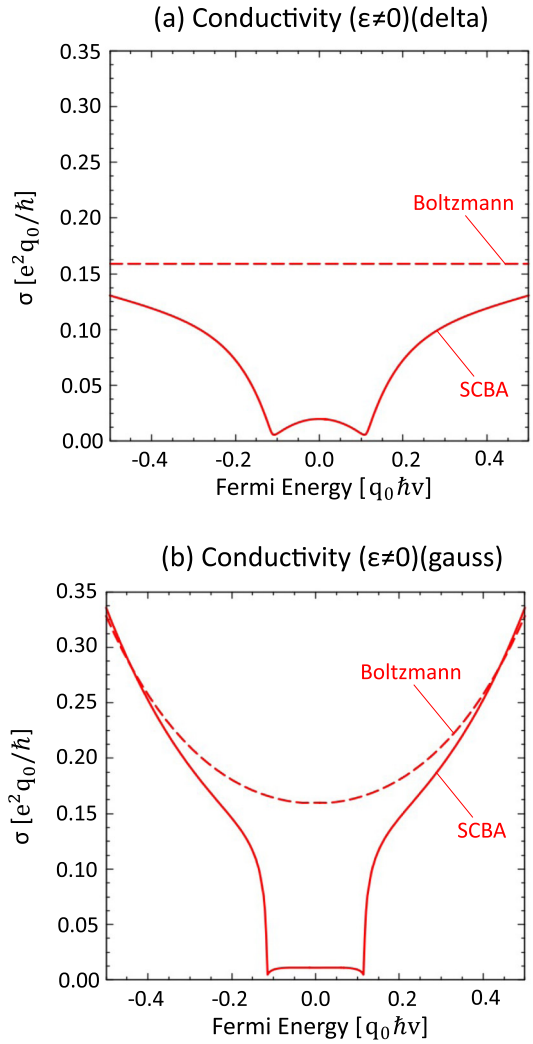

FIG. 5. The conductivity ($W = 2$) derived by the Boltzmann equation (dashed line) and the SCBA (solid line) for (a) the delta function potential and (b) Gaussian potential ($k_c = q_0$).

B. Related studies

In a three-dimensional Weyl fermion under the finite range (Gaussian) impurity potential, the conductivity at the Weyl point changes its behavior significantly depending on the scattering strength, indicating the semimetal–metal transition [30], as Fig. 6 shows. In the spin-1 fermion system, on the contrary, the conductivity at $\epsilon = 0$ has a much smaller dependence on the scattering strength, showing no transition, as Fig. 7 shows.

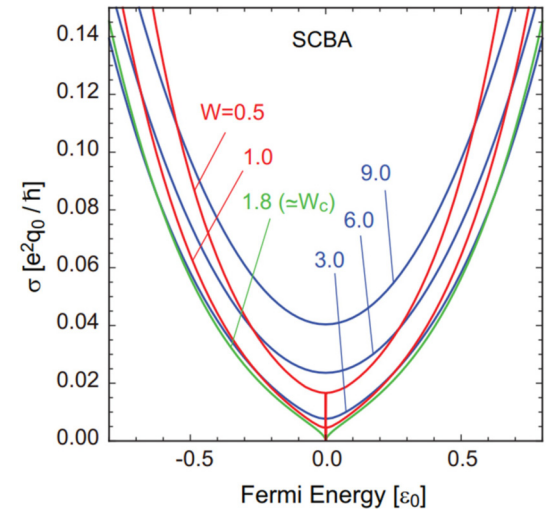

FIG. 6. The conductivity of a three-dimensional Weyl fermion under the Gaussian impurity potential derived by the SCBA, redrawn from [30]. $W = q_0 n_i u_0^2 / 4\pi\hbar^2 v^2$ and $\epsilon_0 = q_0 \hbar v$.

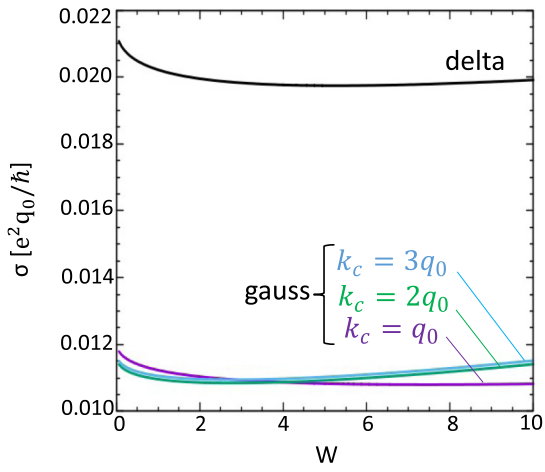

FIG. 7. Conductivity on the zero energy for the delta function potential (black line) and Gaussian potential ($k_c = q_0$: purple line, $k_c = 2q_0$: green line, and $k_c = 3q_0$: blue line) derived by the SCBA.

A spin-1 fermion in two spatial dimensions is not protected by symmetry but approximately emerges. In the two-dimensional spin-1 fermion with the delta-function disorder potential, the density of states has a peak, and the conductivity is suppressed near the zero energy [35] like in the three-dimensional system. The behavior of the conductivity suppression differs between the two-dimensional (2D) and three-dimensional (3D) systems, with the 2D system showing a gradual increase as energy approaches zero, whereas the 3D system shows a rapid increase and makes a small peak. Furthermore, we elucidate a dependence of the lengthscale of the impurity of the conductivity for the three-dimensional system. The short-range (delta function) potential makes a peak, while the finite-range (Gaussian) one does not. This low-energy spectral property of conductivity can be essential to comparing and understanding experimental results in the future.

C. On experimental realization

The present study shows the Fermi-energy dependencies of the density of states and the conductivity. Here we comment on the relation to experimental realization. A direct way to tune the Fermi energy is to use the gating of a thin-film spin-1 fermion material. Alternatively, the Fermi energy could be varied by doping the bulk material, although this is not easy to control continuously. A chiral crystal CoSi hosts a spin-1 chiral fermion on the Brillouin zone center in the absence of spin-orbit interaction, which would be a good platform to observe the quantum transport of the spin-1 fermion. However, in addition to the spin-1 fermion at the Γ point, there is a double Weyl fermion at the R point, and one must take the additional contribution from them into the transport properties. Further research on this is desirable.

VI. CONCLUSION

This study clarifies the quantum transport theory for a spin-1 chiral fermion with disorder potential within the SCBA in the presence of the current vertex correction. As a result, we find some characteristic phenomena originated from the flat-band structure near the zero energy. One is a peak structure of the density of states. The other is the suppression of conductivity. It is discussed that these apparently contradicting behaviors are reconciled by considering the vanishing group velocity of the flat band. In addition, we find that the interband effect, which is inherent to the spin-1 band structure, significantly contributes to the electrical conductivity.

These results provide the basis for clarifying the quantum transport phenomena of spin-1 fermions. Furthermore, it is suggested that nontrivial impurity effects are latent in chiral fermions beyond Dirac and Weyl fermions, and it will be an interesting problem to clarify quantum transport phenomena in more diverse chiral-fermion systems.

Note added. We became aware of a very recent work which studies the density of states [39], Fermi arcs, and surface Berry curvature for the spin-1 chiral fermion in the presence of disorder. We found the same qualitative behavior of the density of states.

ACKNOWLEDGMENTS

This work is supported by JSPS KAKENHI for Grants (Grants No. JP20K03835 and No. JP21K20356) and the Sumitomo Foundation (Grant No. 190228).

APPENDIX A: USEFUL RELATIONS

Let $\boldsymbol{n}_{\perp 1}$, $\boldsymbol{n}_{\perp 2}$, and $\boldsymbol{n}$ be the three-dimensional unit vectors that are perpendicular mutually. Let S_x, S_y, and S_z be the 3×3 spin-1 representation matrices introduced in the main text. We find the following useful relations:

$$(\hat{\boldsymbol{S}} \cdot \boldsymbol{n})^3 = (\hat{\boldsymbol{S}} \cdot \boldsymbol{n}), \tag{A1}$$

$$(\hat{\boldsymbol{S}} \cdot \boldsymbol{n})^2 \hat{S}_i (\hat{\boldsymbol{S}} \cdot \boldsymbol{n})^2 = (\hat{\boldsymbol{S}} \cdot \boldsymbol{n}) \hat{S}_i (\hat{\boldsymbol{S}} \cdot \boldsymbol{n}) = n_i (\hat{\boldsymbol{S}} \cdot \boldsymbol{n}), \tag{A2}$$

$$(\hat{\boldsymbol{S}} \cdot \boldsymbol{n}_{\perp 1})^2 + (\hat{\boldsymbol{S}} \cdot \boldsymbol{n}_{\perp 2})^2 + (\hat{\boldsymbol{S}} \cdot \boldsymbol{n})^2 = 2\hat{S}_0, \tag{A3}$$

$$\begin{aligned}(\hat{\boldsymbol{S}} \cdot \boldsymbol{n}_{\perp 1}) \hat{S}_i (\hat{\boldsymbol{S}} \cdot \boldsymbol{n}_{\perp 1}) + (\hat{\boldsymbol{S}} \cdot \boldsymbol{n}_{\perp 2}) \hat{S}_i (\hat{\boldsymbol{S}} \cdot \boldsymbol{n}_{\perp 2}) \\ + (\hat{\boldsymbol{S}} \cdot \boldsymbol{n}) \hat{S}_i (\hat{\boldsymbol{S}} \cdot \boldsymbol{n}) = \hat{S}_i,\end{aligned} \tag{A4}$$

$$\begin{aligned}(\hat{\boldsymbol{S}} \cdot \boldsymbol{n}_{\perp 1}) \hat{S}_i \hat{S}_j (\hat{\boldsymbol{S}} \cdot \boldsymbol{n}_{\perp 1}) + (\hat{\boldsymbol{S}} \cdot \boldsymbol{n}_{\perp 2}) \hat{S}_i \hat{S}_j (\hat{\boldsymbol{S}} \cdot \boldsymbol{n}_{\perp 2}) \\ + (\hat{\boldsymbol{S}} \cdot \boldsymbol{n}) \hat{S}_i \hat{S}_j (\hat{\boldsymbol{S}} \cdot \boldsymbol{n}) = -\hat{S}_j \hat{S}_i + 2\delta_{ij} \hat{S}_0.\end{aligned} \tag{A5}$$

An arbitrary unit vector $\boldsymbol{n}'$ is expressed as

$$\boldsymbol{n}' = \boldsymbol{n}_{\perp 1} \sin\theta \cos\phi + \boldsymbol{n}_{\perp 2} \sin\theta \sin\phi + \boldsymbol{n} \cos\theta, \tag{A6}$$

where θ denotes the angle between $\boldsymbol{n}$ and $\boldsymbol{n}'$ and ϕ denotes the azimuth angle in the $\boldsymbol{n}_{\perp 1}$-$\boldsymbol{n}_{\perp 2}$ plane.

Using Eqs. (A1) to (A5), we can calculate the following integrals as:

$$\int_0^{2\pi} \int_0^{\pi} d\theta d\phi |u(\boldsymbol{k} - \boldsymbol{k}')|^2 (\hat{\boldsymbol{S}} \cdot \boldsymbol{n}') = (\hat{\boldsymbol{S}} \cdot \boldsymbol{n}) V_1^2(k, k'), \tag{A7}$$

$$\int_0^{2\pi}\int_0^{\pi} d\theta d\phi |u(\boldsymbol{k}-\boldsymbol{k'})|^2(\hat{\boldsymbol{S}}\cdot\boldsymbol{n'})^2 = \left(\frac{3}{2}V_2^2(k,k') - \frac{1}{2}V_0^2(k,k')\right)(\hat{\boldsymbol{S}}\cdot\boldsymbol{n})^2 + \left[V_0^2(k,k') - V_2^2(k,k')\right]\hat{S}_0, \tag{A8}$$

$$\int_0^{2\pi}\int_0^{\pi} d\theta d\phi |u(\boldsymbol{k}-\boldsymbol{k'})|^2 n_x'\hat{S}_0 = V_1^2(k,k')n_x\hat{S}_0, \tag{A9}$$

$$\int_0^{2\pi}\int_0^{\pi} d\theta d\phi |u(\boldsymbol{k}-\boldsymbol{k'})|^2 n_x'(\hat{\boldsymbol{S}}\cdot\boldsymbol{n'}) = \left(\frac{3}{2}V_2^2(k,k') - \frac{1}{2}V_0^2(k,k')\right)n_x(\hat{\boldsymbol{S}}\cdot\boldsymbol{n}) + \frac{1}{2}\left[V_0^2(k,k') - V_2^2(k,k')\right]\hat{S}_x, \tag{A10}$$

$$\int_0^{2\pi}\int_0^{\pi} d\theta d\phi |u(\boldsymbol{k}-\boldsymbol{k'})|^2 n_x'(\hat{\boldsymbol{S}}\cdot\boldsymbol{n'})^2 = \frac{1}{2}[V_1^2(k,k') - V_3^2(k,k')]\hat{S}_x(\hat{\boldsymbol{S}}\cdot\boldsymbol{n}) + \frac{1}{2}\left[V_1^2(k,k') - V_3^2(k,k')\right](\hat{\boldsymbol{S}}\cdot\boldsymbol{n})\hat{S}_x + \left[V_1^2(k,k') - V_3^2(k,k')\right]n_x\hat{S}_0 + \left(\frac{5}{2}V_3^2(k,k') - \frac{3}{2}V_1^2(k,k')\right)n_x(\hat{\boldsymbol{S}}\cdot\boldsymbol{n})^2. \tag{A11}$$

APPENDIX B: BETHE-SALPETER EQUATION

From Appendix A, the Bethe-Salpeter equation becomes Eq. (B1) where $J_i = J_i(k, \epsilon + is0, \epsilon + is'0)$, $J_i' = J_i(k', \epsilon + is0, \epsilon + is'0)$, $V_i^2 = V_i^2(k,k')$, $x = x(k', \epsilon + is0)$, $x' = x(k', \epsilon + is'0)$, and so on,

$$\begin{pmatrix} J_0\\ J_1\\ J_2\\ J_3\\ J_4\\ J_5\\ J_6\\ J_7 \end{pmatrix} = \begin{pmatrix} 1\\ 0\\ 0\\ 0\\ 0\\ 0\\ 0\\ 0 \end{pmatrix} + \int \frac{k'^2dk'}{(2\pi)^3}n_i \begin{pmatrix} V_0^2 & 0 & \frac{1}{2}V_0^2 - \frac{1}{2}V_2^2 & V_0^2 - V_2^2 & V_0^2 - V_2^2 & 0 & 0 & 0\\ 0 & \frac{5}{2}V_3^2 - \frac{3}{2}V_1^2 & 0 & 0 & 0 & 0 & 0 & 0\\ 0 & 0 & \frac{3}{2}V_2^2 - \frac{1}{2}V_0^2 & 0 & 0 & 0 & 0 & 0\\ 0 & 0 & 0 & \frac{3}{2}V_2^2 - \frac{1}{2}V_0^2 & 0 & 0 & 0 & 0\\ 0 & 0 & 0 & 0 & \frac{3}{2}V_2^2 - \frac{1}{2}V_0^2 & 0 & 0 & 0\\ 0 & \frac{1}{2}V_1^2 - \frac{1}{2}V_3^2 & 0 & 0 & 0 & V_1^2 & 0 & 0\\ 0 & \frac{1}{2}V_1^2 - \frac{1}{2}V_3^2 & 0 & 0 & 0 & 0 & V_1^2 & 0\\ 0 & V_1^2 - V_3^2 & 0 & 0 & 0 & 0 & 0 & V_1^2 \end{pmatrix} \hat{T} \begin{pmatrix} J_0'\\ J_1'\\ J_2'\\ J_3'\\ J_4'\\ J_5'\\ J_6'\\ J_7' \end{pmatrix}, \tag{B1}$$

where the matrix $\hat{T}$ is defined as

$$\hat{T} = \begin{pmatrix} xx' & 0 & 0 & 0 & 0 & 0 & 0 & 0\\ T_{01} & T_{11} & T_{21} & T_{31} & T_{41} & T_{51} & T_{61} & T_{71}\\ T_{02} & T_{12} & T_{22} & T_{32} & T_{42} & T_{52} & T_{62} & T_{72}\\ zx' & 0 & 0 & T_{33} & 0 & yx' & 0 & 0\\ xz' & 0 & 0 & 0 & T_{44} & 0 & xy' & 0\\ yx' & 0 & 0 & yx' & 0 & T_{55} & 0 & 0\\ xy' & 0 & 0 & 0 & xy' & 0 & T_{66} & 0\\ 0 & 0 & 0 & 0 & 0 & 0 & 0 & xx' \end{pmatrix}. \tag{B2}$$

Here, the matrix elements T_{ij} in the second line of $\hat{T}$ are given by

$$T_{01} = yz' + zy', \tag{B3}$$

$$T_{11} = xx' + xz' + yy' + zx' + zz', \tag{B4}$$

$$T_{21} = xy' + yx' + yz' + zy', \tag{B5}$$

$$T_{31} = xy' + yz' + zy', \tag{B6}$$

$$T_{41} = yx' + yz' + zy', \tag{B7}$$

$$T_{51} = xz' + yy' + zz', \tag{B8}$$

$$T_{61} = yy' + zx' + zz', \tag{B9}$$

$$T_{71} = xz' + yy' + zx' + zz', \tag{B10}$$

T_{ij} in the third line are given by

$$T_{02} = yy' + zz', \tag{B11}$$

$$T_{12} = xy' + yx' + yz' + zy', \tag{B12}$$

$$T_{22} = xx' + xz' + yy' + zx' + zz', \tag{B13}$$

$$T_{32} = xz' + yy' + zz', \tag{B14}$$

$$T_{42} = yy' + zx' + zz', \tag{B15}$$

$$T_{52} = xy' + yz' + zy', \tag{B16}$$

$$T_{62} = yx' + yz' + zy', \tag{B17}$$

$$T_{72} = xy' + yx' + yz' + zy', \tag{B18}$$

and, the others are given by

$$T_{33} = xx' + zx', \tag{B19}$$

$$T_{44} = xx' + xz', \tag{B20}$$

$$T_{55} = xx' + zx', \tag{B21}$$

$$T_{66} = xx' + xz'. \tag{B22}$$

By solving these eight self-consistent equations, $J_0 - J_7$ are determined.

[1] B. Bradlyn, J. Cano, Z. Wang, M. G. Vergniory, C. Felser, R. J. Cava, and B. A. Bernevig, Beyond dirac and weyl fermions: Unconventional quasiparticles in conventional crystals, Science **353**, aaf5037 (2016).

[2] P. Tang, Q. Zhou, and S.-C. Zhang, Multiple Types of Topological Fermions in Transition Metal Silicides, Phys. Rev. Lett. **119**, 206402 (2017).

[3] D. Takane, Z. Wang, S. Souma, K. Nakayama, T. Nakamura, H. Oinuma, Y. Nakata, H. Iwasawa, C. Cacho, T. Kim, K. Horiba, H. Kumigashira, T. Takahashi, Y. Ando, and T. Sato, Observation of Chiral Fermions with a Large Topological Charge and Associated Fermi-Arc Surface States in CoSi, Phys. Rev. Lett. **122**, 076402 (2019).

[4] D. S. Sanchez, I. Belopolski, T. A. Cochran, X. Xu, J.-X. Yin, G. Chang, W. Xie, K. Manna, V. Süß, C.-Y. Huang, N. Alidoust, D. Multer, S. S. Zhang, N. Shumiya, X. Wang, G.-Q. Wang, T.-R. Chang, C. Felser, S.-Y. Xu, S. Jia *et al.*, Topological chiral crystals with helicoid-arc quantum states, Nature (London) **567**, 500 (2019).

[5] Z. Rao, H. Li, T. Zhang, S. Tian, C. Li, B. Fu, C. Tang, L. Wang, Z. Li, W. Fan, J. Li, Y. Huang, Z. Liu, Y. Long, C. Fang, H. Weng, Y. Shi, H. Lei, Y. Sun, T. Qian *et al.*, Observation of unconventional chiral fermions with long Fermi arcs in CoSi, Nature (London) **567**, 496 (2019).

[6] Q.-Q. Yuan, L. Zhou, Z.-C. Rao, S. Tian, W.-M. Zhao, C.-L. Xue, Y. Liu, T. Zhang, C.-Y. Tang, Z.-Q. Shi, Z.-Y. Jia, H. Weng, H. Ding, Y.-J. Sun, H. Lei, and S.-C. Li, Quasiparticle interference evidence of the topological Fermi arc states in chiral fermionic semimetal CoSi, Sci. Adv. **5**, eaaw9485 (2019).

[7] R. Shen, L. B. Shao, B. Wang, and D. Y. Xing, Single dirac cone with a flat band touching on line-centered-square optical lattices, Phys. Rev. B **81**, 041410(R) (2010).

[8] K. Tang, Y.-C. Lau, K. Nawa, Z. Wen, Q. Xiang, H. Sukegawa, T. Seki, Y. Miura, K. Takanashi, and S. Mitani, Spin Hall effect in a spin-1 chiral semimetal, Phys. Rev. Res. **3**, 033101 (2021).

[9] F. Flicker, F. de Juan, B. Bradlyn, T. Morimoto, M. G. Vergniory, and A. G. Grushin, Chiral optical response of multifold fermions, Phys. Rev. B **98**, 155145 (2018).

[10] M.-Á. Sánchez-Martínez, F. de Juan, and A. G. Grushin, Linear optical conductivity of chiral multifold fermions, Phys. Rev. B **99**, 155145 (2019).

[11] T. Habe, Dynamical conductivity in the multiply degenerate point-nodal semimetal CoSi, Phys. Rev. B **100**, 245131 (2019).

[12] B. Xu, Z. Fang, M.-Á. Sánchez-Martínez, J. W. F. Venderbos, Z. Ni, T. Qiu, K. Manna, K. Wang, J. Paglione, C. Bernhard, C. Felser, E. J. Mele, A. G. Grushin, A. M. Rappe, and L. Wu, Optical signatures of multifold fermions in the chiral topological semimetal CoSi, Proc. Natl. Acad. Sci. **117**, 27104 (2020).

[13] Z. Ni, B. Xu, M.-Á. Sánchez-Martínez, Y. Zhang, K. Manna, C. Bernhard, J. W. F. Venderbos, F. de Juan, C. Felser, A. G. Grushin, and L. Wu, Linear and nonlinear optical responses in the chiral multifold semimetal RhSi, npj Quantum Mater. **5**, 96 (2020).

[14] Z. Ni, K. Wang, Y. Zhang, O. Pozo, B. Xu, X. Han, K. Manna, J. Paglione, C. Felser, A. G. Grushin, F. de Juan, E. J. Mele, and L. Wu, Giant topological longitudinal circular photo-galvanic effect in the chiral multifold semimetal CoSi, Nat. Commun. **12**, 154 (2021).

[15] S. Kaushik and J. Cano, Magnetic photocurrents in multifold Weyl fermions, Phys. Rev. B **104**, 155149 (2021).

[16] B. Dey and T. K. Ghosh, Dynamical polarization, optical conductivity and plasmon mode of a linear triple component fermionic system, J. Phys.: Condens. Matter **34**, 255701 (2022).

[17] S. Nandy, S. Manna, D. Călugăru, and B. Roy, Generalized triple-component fermions: Lattice model, Fermi arcs, and anomalous transport, Phys. Rev. B **100**, 235201 (2019).

[18] G. Chen and C. M. Wang, Optical conductivities in triple fermions with different monopole charges, J. Phys.: Condens. Matter **34**, 105303 (2022).

[19] O. Pal, B. Dey, and T. K. Ghosh, Berry curvature induced anisotropic magnetotransport in a quadratic triple-component fermionic system, J. Phys.: Condens. Matter **34**, 155702 (2022).

[20] P. Hosur and X. Qi, Recent developments in transport phenomena in Weyl semimetals, C. R. Phys. **14**, 857 (2013).

[21] N. P. Armitage, E. J. Mele, and A. Vishwanath, Weyl and Dirac semimetals in three-dimensional solids, Rev. Mod. Phys. **90**, 015001 (2018).

[22] E. V. Gorbar, V. A. Miransky, I. A. Shovkovy, and P. O. Sukhachov, *Electronic Properties of Dirac and Weyl Semimetals* (World Scientific, Singapore, 2020).

[23] E. Fradkin, Critical behavior of disordered degenerate semiconductors. II. Spectrum and transport properties in mean-field theory, Phys. Rev. B **33**, 3263 (1986).

[24] A. W. W. Ludwig, M. P. A. Fisher, R. Shankar, and G. Grinstein, Integer quantum hall transition: An alternative approach and exact results, Phys. Rev. B **50**, 7526 (1994).

[25] N. H. Shon and T. Ando, Quantum Transport in Two-Dimensional Graphite System, J. Phys. Soc. Jpn. **67**, 2421 (1998).

[26] K. Ziegler, Delocalization of 2D Dirac Fermions: The Role of a Broken Supersymmetry, Phys. Rev. Lett. **80**, 3113 (1998).

[27] J. Tworzydło, B. Trauzettel, M. Titov, A. Rycerz, and C. W. J. Beenakker, Sub-Poissonian Shot Noise in Graphene, Phys. Rev. Lett. **96**, 246802 (2006).

[28] M. I. Katsnelson, Zitterbewegung, chirality, and minimal conductivity in graphene, Eur. Phys. J. B **51**, 157 (2006).

[29] M. Noro, M. Koshino, and T. Ando, Theory of Transport in Graphene with Long-Range Scatterers, J. Phys. Soc. Jpn. **79**, 094713 (2010).

[30] Y. Ominato and M. Koshino, Quantum transport in a three-dimensional weyl electron system, Phys. Rev. B **89**, 054202 (2014).

[31] K. Kobayashi, T. Ohtsuki, K.-I. Imura, and I. F. Herbut, Density of States Scaling at the Semimetal to Metal Transition in Three Dimensional Topological Insulators, Phys. Rev. Lett. **112**, 016402 (2014).

[32] R. Nandkishore, D. A. Huse, and S. L. Sondhi, Rare region effects dominate weakly disordered three-dimensional Dirac points, Phys. Rev. B **89**, 245110 (2014).

[33] Y. Ominato and M. Koshino, Quantum transport in three-dimensional weyl electron system in the presence of charged impurity scattering, Phys. Rev. B **91**, 035202 (2015).

[34] Y. Ominato and M. Koshino, Magnetotransport in Weyl semimetals in the quantum limit: Role of topological surface states, Phys. Rev. B **93**, 245304 (2016).

[35] M. Vigh, L. Oroszlány, S. Vajna, P. San-Jose, G. Dávid, J. Cserti, and B. Dóra, Diverging dc conductivity due to a flat band in a disordered system of pseudospin-1 dirac-weyl fermions, Phys. Rev. B **88**, 161413(R) (2013).

[36] W. Häusler, Flat-band conductivity properties at long-range Coulomb interactions, Phys. Rev. B **91**, 041102(R) (2015).

[37] Z. Yang, W. Chen, Q. W. Shi, and Q. Li, Quantum conductivity correction in a two-dimensional disordered pseudospin-1 system, Phys. Rev. B **99**, 134204 (2019).

[38] R. Burgos, J. H. Warnes, and G. C. Arteaga, Semiclassical anisotropic transport theory in two dimensional pseudo-spin one system, Phys. E **136**, 114998 (2022).

[39] H.-C. Hsu, I. C. Fulga, and J.-S. You, Disorder effects on triple point fermions, arXiv:2205.12003.